



Structural dynamics of nanoscale gold by ultrafast electron crystallography

Sascha Schäfer, Wenxi Liang, Ahmed H. Zewail*

Physical Biology Center for Ultrafast Science and Technology, Arthur Amos Noyes Laboratory of Chemical Physics, California Institute of Technology, Pasadena, CA 91125, United States

ARTICLE INFO

Article history:

Received 24 August 2011

In final form 16 September 2011

Available online 21 September 2011

ABSTRACT

By employing ultrafast electron crystallography in a transmission geometry for ultra-thin (2–3 nm) gold, here we show that structural dynamics of the transverse atomic motions and the atomic displacements around the equilibrium position can be separated from the measured change in Bragg diffraction, the positions and intensities of the peaks, respectively. The rate of intensity change provides the electron-lattice equilibration time whereas the observed lattice expansion, which occurs on a slower time scale, maps the delayed response of transverse lattice strain. These textbook-type results provide the microscopic stress–strain profile that is critical for understanding dynamical deformations and the effect of morphological structures at surfaces.

© 2011 Elsevier B.V. All rights reserved.

1. Introduction

In simple metals, like gold, when excited, the equilibration of electrons with the lattice occurs on the ultrashort time scale [1,2]. Typically, such equilibration is measured using spectroscopic pump–probe techniques which are predominantly sensitive to the relaxation dynamics of the electronic system, although with dependence on structural changes [3]. This is because the wavelength of light far exceeds interatomic distances. The spectroscopic experiments established the time scales of electron–electron and electron–phonon scatterings, and critically assessed the applicability of a simple theoretical description, the two-temperature model [4], which separates the electrons and the lattice into two sub-systems.

With the advent of ultrafast diffraction techniques using short X-ray or electron pulses [5,6] as a direct probe to lattice dynamics, there is a renewed interest in the structural aspects of the ultrafast dynamics of metal films, both experimentally [7–11] and theoretically [12–14]. These studies have explored, among others, non-thermal melting dynamics [7], electronically and thermally driven lattice expansions [8,10,11], and excited state bonding changes [15]. By using diffraction-contrast in ultrafast electron microscopy, it was also possible to directly image the nanoscale surface bending and lattice expansion on the ultrashort time scale and with nanometer resolution [16,17].

Here, we study the ultrafast dynamics of gold films having a thickness of 2–3 nm. We place special emphasis on the quantitative interpretation of the observed diffraction characteristics and the fluence-dependent rates of lattice heating and expansion. We show that lattice heating dynamics proceed on a slower time scale

with the increase of fluence, in agreement with results we obtained using the two-temperature model. The experimentally observed rates of lattice expansion can be understood by examining the nature of the temporal stress–strain relationship. Because the electron pulse propagates perpendicular to the gold surface, it was possible to study the transverse expansion of the lattice. The results reported here are significant for other applications as they provide clear evidence of structural dynamics, and the relationship to directionality of atomic motions and strain propagation.

2. Methodology

The Caltech apparatus has been described elsewhere [5,18]; here, the transmission mode of diffraction was utilized. Structural dynamics were initiated by an 800 nm laser pulse, with a pulse width of ~100 fs, and electron diffraction patterns were recorded at well-defined delay times, t , after excitation, utilizing the sub-ps electron pulses described in Ref. [19]. In Figure 1 (left panel), the recorded diffraction pattern and in Figure 1 (middle panel) the change of the diffraction pattern after excitation are depicted. The diffraction pattern (Figure 1 left panel, inset) consists of Debye–Scherer rings since the film contains randomly oriented crystallites. The radially-averaged pattern shows a series of peaks which can be assigned to the allowed Laue diffraction peaks of the face-centered cubic lattice structure of gold.

As shown in Figure 1 (middle panel), laser excitation leads to a decrease of the ring intensity, whereas between the rings (background) the number of scattered electrons increases. Additionally, there is a contraction of the diffraction rings after excitation, which may not be directly visible to the naked eye. In order to quantify the laser-induced temporal changes, we radially averaged each diffraction pattern at a given delay time t and fitted a Lorentzian function to the individual diffraction peaks together with a

* Corresponding author. Fax: +1 626 792 8456.

E-mail address: zewail@caltech.edu (A.H. Zewail).

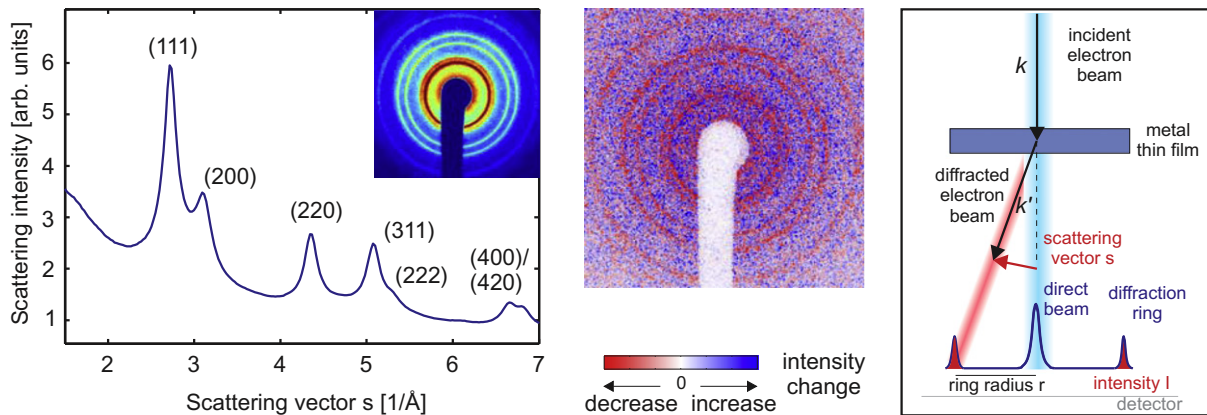


Figure 1. Radially averaged diffraction pattern of nanoscale gold and electron diffraction geometry. (left panel) The diffracted intensity at a scattering vector s is obtained by averaging the Debye-Scherrer rings in the original diffraction pattern (inset). The maxima in the scattered intensity are labeled according to the corresponding reciprocal lattice points. (middle panel) The laser-induced change of the diffraction pattern at $t = 1$ ns, which shows a decrease of the Debye-Scherrer ring intensity and an increase in the background intensity, as well as ring contraction. (right panel) The incidence electron beam direction is perpendicular to the specimen surface. A diffracted beam is formed with a wave vector $k' = k + s$, where the scattering vector s is nearly parallel to the surface (see text). From the intensity and the radius of the corresponding diffraction ring, which is formed at the detector, transverse lattice expansion and lattice heating can be obtained.

piecewise-linear background. For every delay time we recorded 40 diffraction patterns, each one averaged over 2.5×10^4 electron pulses.¹

From the fitted Lorentzian functions we deduced the position, $r(t)$, and the integrated intensity, $I(t)$, of the diffraction peaks in the radially averaged pattern at the different delay times. To rule out possible artifacts from peak fitting, we also considered the summed intensity under each group of overlapping peaks (subtracted by a linear background) as a measure of the scattered intensity. This procedure gave identical results for the intensity decrease to those obtained from the fitted peaks themselves (see below). The change in the background intensity was obtained by integrating the intensity between the (200) and (220) peaks (i.e., for the following range of scattering vectors: $3.5 \text{ \AA}^{-1} < s < 3.9 \text{ \AA}^{-1}$).

The nanoscale gold films, which were investigated here, are commercially available (Ted Pella Inc, Substrattec grid) and have a thickness of 2–3 nm. The crystalline domains have a size of ~ 5 nm, and the transverse grain size is on the order of 25–50 nm, as observed in transmission electron microscopy, which was provided by the supplier.

3. Diffraction and structural dynamics

As shown in Figure 1 (right panel), the incident electron beam with a wave vector k scatters due to the interaction with the metal thin film into a set of diffracted electron beams (for clarity, only one diffracted beam with a wave vector k' is shown). For elastic scattering, the energy of the diffracted electrons is equal to the incident one, and thus $|k| = |k'|$. The scattering vector s , which is defined by $k' - k$, signifies the momentum transfer between the lattice and the probing electron beam. From a simple geometrical consideration, the angle between s and k is $90^\circ - \theta$, where 2θ denotes the scattering angle (i.e., angle between k and k'). Therefore, taking typical values of $2\theta \approx 5^\circ$ into account, s can be considered almost perpendicular to k .

¹ Every diffraction pattern was radially-averaged and the intensity, position and width of the diffraction peaks were obtained. Small drifts during the acquisition period are compensated for by third order polynomials that describe the temporal behavior (intensity and position) of the incident electron beam in time. For every diffraction pattern the center was individually determined by a Hough transform in order to compensate for any small shift of the electron beam, including the effect of laser-induced electric fields [20], which was found to be very small, on the order of a pixel at most.

Experimentally, the intensity of scattered electrons, $I(s)$, depends on s , and is detected on the CCD in the far-field. Because θ is very small, a linear relationship follows between the position on the detector and the scattering vector, s , in the far-field. In our case, the metal film studied is polycrystalline and therefore macroscopically isotropic resulting in a diffraction pattern with radial symmetry. It is thus sufficient to describe the position on the detector by a radius r .

The observed intensity is directly related to the time-dependent structure factor, $F(t)$, which contains the atomic displacements $u_j(t)$; in the kinematical scattering regime [21], $I(t)$ is simply the square of the structure factor, i.e., $I(t) \propto |F(t)|^2$. The structure factor is given by

$$F(t) = \sum_j f_j \exp [is \cdot (R_j + u_j(t))], \quad (1)$$

where R_j denotes the equilibrium position of the j -th atom and f_j is its atomic scattering factor. The summation runs over all atoms j in the sample within the coherence volume of the electron beam. Since both s and $u_j(t)$ are vectorial quantities, only the component of $u_j(t)$ which is parallel to s (i.e., approximately perpendicular to k) leads to a temporal change of the structure factor and thus to a temporal change of the diffraction pattern. Furthermore, a homogeneous displacement (i.e., $u_j(t)$ is independent of j) only contributes a phase factor to F and does not therefore lead to changes in the diffraction pattern. In contrast, it is the inhomogeneous change of the time-dependent displacement field that is of interest; for example in heating the solid, the atomic displacements are not uniform and in-fact $u_j(t)$ linearly changes with atomic position, but for coherent phonons $u_j(t)$ can oscillate. Two quantities, which can be directly extracted from the time-dependent change of the diffraction pattern, are the temporal change of the atomic mean-square displacement, $\Delta \langle u^2 \rangle_t$, and the average change in the interatomic distances, $\langle (u_i - u_j) / (R_i - R_j) \rangle_t$. In both cases, the average denoted by $\langle \cdot \rangle$ is taken over all indices (i, j) and only the components parallel to s need to be considered.

For a crystalline sample, as it is studied here, the change in the interatomic distances can be obtained by considering the scattering vectors, s , which give a maximum in the scattered electron intensity $I(s)$ (Debye-Scherrer rings). These scattering vectors satisfy the Bragg condition, $s = 2\pi/d$, where d is the distance between crystallographic planes within the sample. Temporal changes in the interatomic distances therefore lead to a change in the Bragg

condition and thus to a change in the radius of the Debye-Scherer rings. Using the connection between the interplanar distance and the scattering vector, we obtain the following relations between the temporal change in the ring radius, $\Delta r(t)$, and the dynamical change of the interplanar distances Δd :

$$\frac{\Delta r(t)}{r(t < 0)} = -\frac{\Delta d(t)}{d(t < 0)}. \quad (2)$$

Here, $t < 0$ indicates the corresponding quantities before laser excitation (static case).

Similarly, the time-dependent increase of the atomic mean-square displacement $\Delta \langle u^2 \rangle_t$ is connected to a decrease in the intensity of diffraction peaks due to the Debye-Waller effect, i.e.,

$$\ln \left[\frac{I(t)}{I(t < 0)} \right] = -\frac{s^2 \Delta \langle u^2 \rangle_t}{3}. \quad (3)$$

4. Results and discussion

In Figure 2, we show the temporal change of the intensity and position of the (220)-ring, together with the time-dependent increase of the background intensity at an excitation energy of 50 $\mu\text{J}/\text{pulse}$ (corresponding to a fluence of $\sim 1.5 \text{ mJ}/\text{cm}^2$). All three transients can be well described by single-exponential functions, albeit with different time constants τ . The intensity change exhibits the fastest dynamics with a time constant of $\tau_{\langle u^2 \rangle} = 11.5 \pm 1 \text{ ps}$, whereas the increase of the background intensity and the decrease of the (220)-ring radius occur with longer time constants: $\tau_B = 18 \pm 2 \text{ ps}$, and $\tau_r = 22 \pm 2 \text{ ps}$, respectively. For delay times up to $t = 900 \text{ ps}$, no further change in the diffraction pattern was visible, consistent with cooling being on a longer time scale and that at $\sim 1 \text{ ns}$ the system did not begin its recovery to the initial structure; transverse heat diffusion is estimated to occur on the order of microseconds.

The temporal changes in the diffraction patterns are unambiguously identifiable with structural dynamics. This is made by checking for the order-dependence of the relative intensity change ($\propto s^2$,

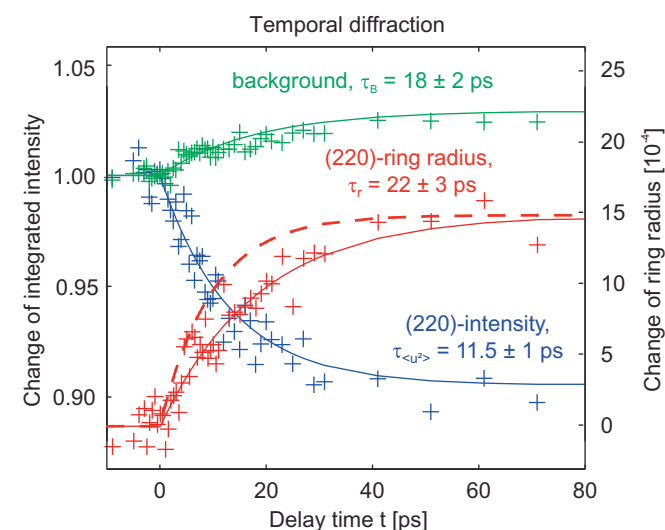


Figure 2. Diffraction changes of the (220)-ring, and the background. The experimentally observed time-dependent change of the (220)-ring radius (red crosses), the (220) intensity (blue crosses) and the background intensity between the (200)- and (220)-ring (green crosses) are fitted by monoexponential functions (solid curves); for comparison, we display (broken, red curves) a fit to the change of ring radius if τ_r equals to 11.5 ps, the same value as that of the intensity decay. The change of integrated intensity and ring radius are defined as $I(t)/I(t < 0)$ and $\Delta r(t)/r(t < 0)$, respectively (see Eqs. 2 and 3).

Eq. 3), and by the relative change in the ring radius (independent of s , Eq. 2), both examined for different fluences, as depicted in Figure 3. We note that the former change we refer to is the integrated intensity, as dictated by the Debye-Waller theory; the height of diffraction peaks (not shown) may not follow a simple s^2 -dependence due to a contribution from a time-dependent peak broadening [9].

Using the asymptotic values of the exponential fits, it is also possible to estimate the temperature jump induced by the laser excitation. By invoking the Debye-model to describe the temperature dependent vibrational excitation, with a Debye temperature of $T_D = 165 \text{ K}$ for gold, we obtained for the intensity decrease (at plateau) of $11.6 \pm 0.5\%$, for the (311)-ring, a temperature increase of $\Delta T = 177 \pm 8 \text{ K}$, at the highest fluence given. The temperature could also be estimated from the observed lattice expansion of $0.135 \pm 0.01\%$. Using the bulk thermal expansion coefficient $\alpha = 14.2 \times 10^{-6}/\text{K}$ [22], would give $\Delta T = 95 \pm 7 \text{ K}$ in contrast to the temperature obtained from the intensity decrease. However, it is known that nanoscale gold particles show a decreased thermal expansion coefficient when compared to the corresponding bulk value [23]. With the temperature rise obtained from the intensity decrease, we conclude that for the nanoscale gold the thermal expansion coefficient is $7.6 \pm 0.7 \times 10^{-6}/\text{K}$, which is well within the experimental results reported before for nanoparticles studied by static X-ray absorption fine structure measurements at different temperatures [23].

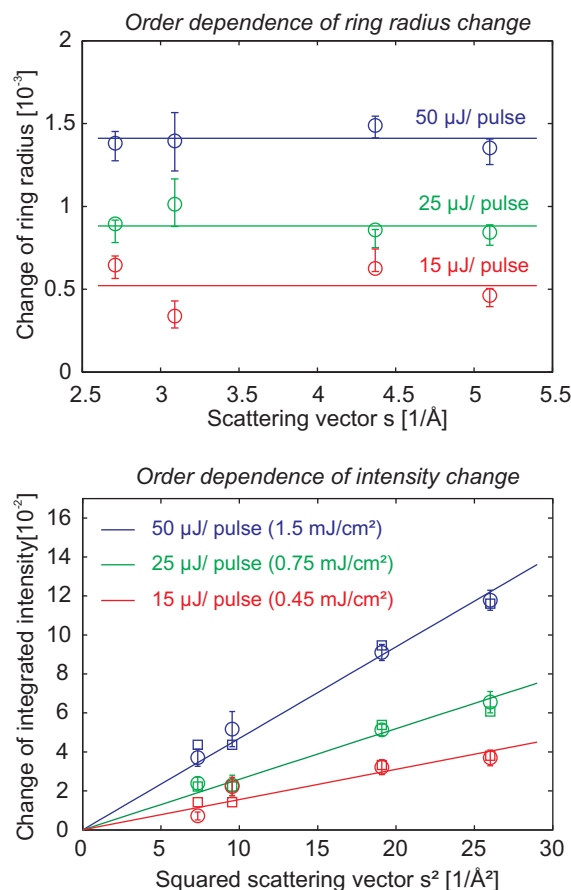


Figure 3. Order dependence of diffraction ring contraction and intensity decrease. (upper panel) The relative change of the ring radius at long delay times, $\Delta r/r$, is shown for different Debye-Scherer rings with scattering vector s at excitation energies of 15 (red circles), 25 (green circles) and 50 $\mu\text{J}/\text{pulse}$ (blue circles). The relative change $\Delta s/s$ does not depend on s . (lower panel) The corresponding intensity decrease of the Debye-Scherer rings shows a quadratical dependence on the scattering vector, as theoretically expected (see text).

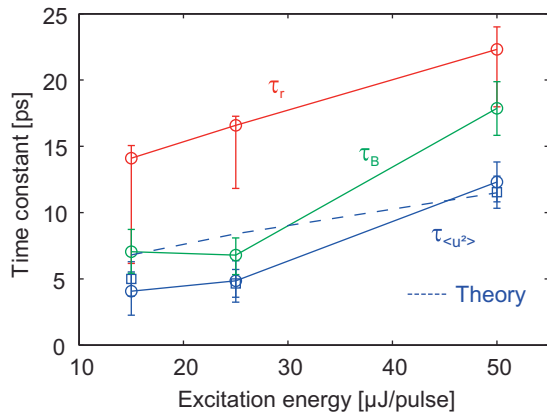


Figure 4. Time constants of structural dynamics and their fluence dependence. The time constants for the lattice expansion (red circles), the increase of the mean square displacement (blue circles) and for the increase of the scattered background intensity (green circles) are compared at different excitation energies per pulse. The broken line denotes the results of a numerical simulation employing the two-temperature model (see text for details). To exclude possible artifacts from the data fitting procedure, we also considered the dynamics of the intensity of the Debye-Scherrer rings by directly summing the scattered electron intensity of the individual groups of overlapping rings (blue squares).

Figure 4 depicts the experimentally observed fluence dependence of the time constants $\tau_{\langle u^2 \rangle}$, τ_r and τ_B . First, we consider the fluence dependence of the intensity change ($\tau_{\langle u^2 \rangle}$) by invoking the two-temperature model [4], which assumes that electron and lattice sub-systems are in a pseudo-equilibrium, defined by electron and lattice temperatures, T_e and T_l , respectively. Physically, the clocking laser pulse leads to an excitation of the specimen to levels above the Fermi surface. Following electron–electron scattering events, which typically occur on a 1–100 fs time scale, the system can be characterized by a pseudo-equilibrium electron sub-system at an elevated electron temperature T_e and a ‘cold’ lattice. Subsequently, energy is transferred to the lattice sub-system on a time scale which is determined by the electron–phonon coupling constant g . The excitation of the lattice sub-system can be described by an increased lattice temperature T_l , which leads to the experimentally observed increase of the atomic mean-square displacement $\Delta\langle u^2 \rangle$.

In the limit of a small excitation, i.e., if the increase in the electron temperature, ΔT_e , is small compared to the initial electron temperature, $T_{e,0}$, i.e., $\Delta T_e \ll T_{e,0}$, the time constant for the electron–phonon equilibration is given by $\tau = C_e/g$, where C_e is the electron heat capacity. In most spectroscopic pump–probe experiments the fluence is relatively low and in this regime $g = 2.6 \times 10^{16} \text{ W}/(\text{m}^3 \cdot \text{K})$ and $C_e = 18 \text{ kJ}/(\text{m}^3 \cdot \text{K})$ [24], thus giving the electron–phonon coupling time to be 700 fs. However, since C_e depends nearly linearly on the electronic temperature T_e (i.e., $C_e = C_{e,0}T_e$), τ should lengthen at higher fluences.

The broken blue line in Figure 4 gives the calculated $\tau_{\langle u^2 \rangle}$, obtained by solving the two-temperature equations, and giving $g = 9.5 \times 10^{15} \text{ W}/(\text{m}^3 \cdot \text{K})$ when the electron heat capacity is taken from the literature [24]. The absorbed energy was deduced from the experimentally observed asymptotic temperature increase, as determined by the intensity change. The electron–phonon coupling constant for bulk gold is reported to be $g = 2.6 \times 10^{16} \text{ W}/(\text{m}^3 \cdot \text{K})$, significantly larger than that given here. This difference may reflect the effect of confinement on the nanoscale. We note that $\tau_{\langle u^2 \rangle}$ is shorter than τ_B , and this is because the latter contains in addition to electron–phonon dynamics other factors such as the temporal change of plasmon scattering and diffuse scattering from defects [25]. A slower increase of the background intensity compared to the decrease of the diffraction intensity, i.e.,

$\tau_{\langle u^2 \rangle} < \tau_B$, as observed here, was also found in a previous study on the melting dynamics of gold [7].

As shown in Figures 2 and 4, the lattice expansion proceeds on a slower time scale than that of the intensity change. One might presume that it is only the initial lattice heating that causes the expansion. However, it has been shown that at very low temperatures, when the atoms are nearly at rest, expansion can occur as a result of an electron temperature alone, in this case acting as a pressure on the atoms. In general, therefore, the laser-induced stress can be written as [3]

$$\sigma(t) = \frac{1}{3}(\gamma_e \Delta E_e + \gamma_l \Delta E_l), \quad (4)$$

with the electronic and lattice Grueneisen constants of gold, having the values $\gamma_e = 1.6$ and $\gamma_l = 2.96$ [26]. We note that the Grueneisen constants, $\gamma_{e,l}$, are given by the thermodynamic change of pressure with energy at a fixed volume, i.e., $\gamma = V(\partial p/\partial E)_V$, which implies equilibrium values for a given t , a condition that may not in general hold.

The energies, ΔE_e and ΔE_l , are the excitations stored in the electronic and lattice systems, respectively. With an initial excitation in the electron sub-system, $\Delta E_l = 0$. However, on the time scale of the electron–phonon coupling there is a contribution from both.

It follows that the dynamics of the induced stress $\sigma(t)$ contains a fast component due to the initial increase of the electronic temperature T_e and a slower component caused by the increased lattice temperature through electron–phonon coupling. The generated strain (i.e., lattice expansion or contraction) is what is observed in diffraction. From knowledge of the temporal stress profile, $\sigma(t)$, we can then obtain the spatial strain and its evolution with time.

Taking into account the transverse grain size of $l \sim 40 \text{ nm}$, we expect that the lattice response time to be on the order of l/v_s , where v_s is the sound velocity. With $v_s = 3160 \text{ m/s}$ for gold [22], we obtained a temporal delay between stress and strain of $\sim 13 \text{ ps}$, which is close to the observed value. Given that the 13 ps is for an impulsive stress and that the time constant of the lattice heating is $\tau_{\langle u^2 \rangle} = 11.6 \pm 0.5 \text{ ps}$ (at the highest fluence), the combination (convolution) can qualitatively explain the delayed lattice expansion observed experimentally. We note that the lattice expansion in the normal direction to the film (perpendicular to the surface) is expected to occur on a time scale of $\sim 1 \text{ ps}$ because in this direction the film thickness is 3 nm. However, a diffraction geometry with near-normal incidence of the probing electron beam, as employed here, is not sensitive to this direction, as mentioned above. As shown by [17], the lateral breathing mode of a graphite film can be observed when an inclined probing direction is invoked.

For more quantification of stress–strain dynamics we used finite-element simulations², first considering a simplified cylindrically shaped gold grain with a diameter of 40 nm (Figure 5, upper panel). For a more realistic shape (Figure 5, lower panel) we considered a mimic of what was observed in transmission electron microscopy of the thin film sample. The mimic is a representative example of the grains which are present in the sample, both in shape and size. The strain dynamics for both the cylindrical and the irregular-shaped particles was examined taking into consideration three different models for the temporal stress build-up, as depicted in Figure 5 (lower panel, inset). In the first case (blue curves), γ_e and γ_l are taken to be equal, leading to a rise time for the stress that is similar to the laser pulse width. The second case utilizes the experimental values for the Grueneisen constants (see above), and the third case signifies a thermal expansion solely caused by the increase of the lattice temperature.

² For the finite element simulation, we used the Comsol 4.2 software package. All material constants are taken to be equal to that of the bulk.

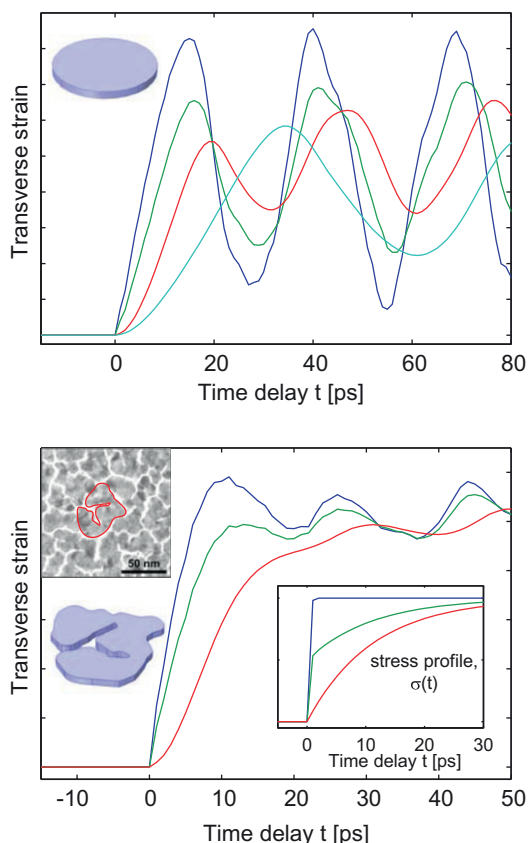


Figure 5. Temporal stress–strain relationship. By employing structural finite-element simulations for a cylindrical particle (diameter 40 nm, thickness 3 nm, upper panel) and an irregular shaped particle (overall diameter ~60 nm, thickness 3 nm, lower panel) we obtained the temporal evolution of the transverse strain (lattice expansion parallel to the film surface) for the three different stress models shown in the inset of the lower panel (see text for details). The irregular shaped particle mimics the grain shape as obtained by transmission electron microscopy (inset, lower panel, see text).

As can be seen in Figure 5, the temporal behavior of the lattice expansion (relative strain) depends on both the intrinsic properties of the material (size and shape of the grain particles) and the nature of the temporal stress imposed on the material. Interestingly, the simulated strain responses still show somewhat faster time-constants when compared to the experimental results. However, this is expected since the individual grains in the thin film are not isolated but interconnected by semi-amorphous boundaries which limit the transverse lattice expansion of a single grain. Due to this interconnection of several grains, we expect that the effective length scale for the structural response is larger than the size of an individual grain. Taking for example a cylindrical-shaped particle with a diameter of 80 nm (Figure 5, cyan curve, using the second strain model) would give a structural response time on the order of ~20 ps in agreement with the experimental results.

5. Conclusion

Using time-resolved electron diffraction of nanoscale metals we have shown the unique features of structural dynamics, separating the time scale of lattice heating from structural expansion, and providing an understanding of the microscopic stress–strain temporal evolution. The lattice expansion lags significantly behind its heating which is addressed here by using structural finite element simulations. The results indicate the critical role of morphological structures at the surface in determining the temporal stress–strain relationship, which depends on the transverse grain size and material properties. These effects, which have to be considered in future studies of complex systems, signify the importance of microscopic dynamics in controlling macroscopic properties.

Acknowledgments

This work was supported by the National Science Foundation and the Air Force Office of Scientific Research in the Center for Physical Biology at Caltech supported by the Gordon and Betty Moore Foundation. One of the authors (S.S.) gratefully acknowledges a scholarship from the Alexander von Humboldt-Foundation.

References

- [1] J. Hohlfield, S.S. Wellershoff, J. Güdde, U. Conrad, V. Jahnke, E. Matthias, *Chem. Phys.* 251 (2000) 237.
- [2] H.E. Elsayed-Ali, T. Juhasz, G.O. Smith, W.E. Bron, *Phys. Rev. B* 43 (1991) 4488.
- [3] C. Thomsen, H.T. Grahn, H.J. Maris, J. Tauc, *Phys. Rev. B* 34 (1986) 4129.
- [4] S.I. Anisimov, B.L. Kapeliovich, T.L. Perelman, *Sov. Phys. JETP* 39 (1974) 375.
- [5] A.H. Zewail, J.M. Thomas, *4D Electron Microscopy: Imaging in Space and Time*, Imperial College Press, London, 2010 (and references therein).
- [6] M. Chergui, A.H. Zewail, *ChemPhysChem* 10 (2009) 28, and references therein.
- [7] R. Ernstorfer, M. Harb, C.T. Hebeisen, G. Sciaini, T. Dartigalongue, R.J.D. Miller, *Science* 323 (2009).
- [8] S. Nie, X. Wang, H. Park, R. Clinite, J. Cao, *Phys. Rev. Lett.* 96 (2006) 025901.
- [9] M. Ligges, I. Rajkovic, P. Zhou, O. Posth, C. Hassel, G. Dumpich, D. von der Linde, *Appl. Phys. Lett.* 94 (2009) 101910.
- [10] M. Nicoul, U. Shymanovich, A. Tarasevitch, D. von der Linde, K. Sokolowski-Tinten, *Appl. Phys. Lett.* 98 (2011) 191902.
- [11] J. Chen, W.K. Chen, P.M. Rentzepis, *J. Appl. Phys.* 109 (2011) 113522.
- [12] D.S. Ivanov, L.V. Zhigilei, *Phys. Rev. B* 68 (2003) 064114.
- [13] Z. Lin, L.V. Zhigilei, *J. Phys.: Conf. Ser.* 59 (2007) 11.
- [14] J. Li, R. Clinite, X. Wang, J. Cao, *Phys. Rev. B* 80 (2009) 014304.
- [15] G. Sciaini et al., *Nature* 458 (2009) 56.
- [16] B. Barwick, H.S. Park, O.-H. Kwon, J.S. Baskin, A.H. Zewail, *Science* 322 (2008) 1227.
- [17] H.S. Park, J.S. Baskin, B. Barwick, O.-H. Kwon, A.H. Zewail, *Ultramicroscopy* 110 (2009) 7.
- [18] C.-Y. Ruan, F. Vigliotti, V.A. Lobastov, S. Chen, A.H. Zewail, *Proc. Natl. Acad. Sci.* 101 (2004) 1123.
- [19] S. Schäfer, W. Liang, A.H. Zewail, *New J. Phys.* 13 (2011) 063030.
- [20] S. Schäfer, W. Liang, A.H. Zewail, *Chem. Phys. Lett.* 493 (2010) 11.
- [21] M. de Graef, *Introduction to Conventional Transmission Electron Microscopy*, Cambridge University Press, Cambridge, 2003.
- [22] D. Lide (Ed.), *CRC Handbook of Chemistry and Physics*, 85th ed., CRC Press, Boca Raton, 2005.
- [23] T. Comaschi, A. Balerna, S. Mobilio, *Phys. Rev. B* 377 (2008) 075432.
- [24] Z. Lin, L.V. Zhigilei, V. Celli, *Phys. Rev. B* 77 (2008) 075133.
- [25] Z.L. Wang, *Elastic and inelastic scattering in electron diffraction and imaging*, Plenum Press, New York, 1995.
- [26] K.O. McLean, C.A. Swenson, C.R. Case, *J. Low Temp. Phys.* 7 (1972) 77.